Investigation of the Unsteady Behaviour of a Laminar Separation Bubble Using Infrared Thermography

Adrián Grille Guerra[1,2,*], Christoph Mertens[1], Jesse Little[2], Bas W. van Oudheusden[1]

1: Faculty of Aerospace Engineering, Delft University of Technology, The Netherlands
2: Dept. of Aerospace and Mechanical Engineering, The University of Arizona, United States
*Corresponding author: adrigrille13@gmail.com

Keywords: Differential Infrared Thermography, Unsteady Aerodynamics, Laminar Separation Bubble

ABSTRACT

The laminar separation bubble (LSB) that forms on the suction side of a modified NACA $64_3 - 618$ airfoil at a chord-based Reynolds number of $Re = 200k$ is studied using wind tunnel experiments. First, the LSB is characterized over a range of static angles of attack, using surface pressure measurements and infrared thermography (IT). For the conditions tested, excellent agreement between the techniques is obtained, showing an upstream shift of the bubble with increasing angle of attack. For the study of steady LSBs, the infrared approach is superior, given its higher spatial resolution and experimental simplicity. The complexity is then increased to study the influence of aerodynamic unsteadiness on the bubble. For this purpose, a pitching-type motion is imposed on the wind tunnel model, testing reduced frequencies up to $k = 0.25$. While surface pressure measurements are not affected by the change in experimental conditions, the infrared approach is limited by the thermal response of the surface. To overcome this limitation, an extension of the recently proposed differential infrared thermography (DIT) method is considered. With this method, the unsteady behavior of the LSB can be partially detected. Both experimental techniques indicate a hysteresis in bubble location between the pitch up and pitch down parts of the motion, caused by the effect of the aerodynamic unsteadiness on the adverse pressure gradient. However, the DIT measurements indicate a larger hysteresis, which is attributed to the thermal response time of the model surface.

1. Introduction

Unmanned aerial vehicles (UAVs) have proliferated in the last few decades, with applications that include military, commercial and recreational. The size and typical flight velocities of UAVs is characterized by moderate Reynolds numbers $O(10^4 - 10^5)$. At such low Reynolds numbers, boundary layers can remain laminar, which makes them highly susceptible to separation, leading to the generation of laminar separation bubbles (LSBs). Gaster (1967) and Horton (1968) were among the first to study LSBs, investigating the effect of pressure gradient and Reynolds number on the nature and size of the bubble. They defined the three characteristic features of LSBs, which are the

separation of the laminar boundary layer due to the adverse pressure gradient, the transition to turbulence within the separated shear layer that encloses the bubble, and the reattachment of the turbulent boundary layer.

Extensive research has been done to study the influence of various parameters, such as Reynolds number (Burgmann & Schröder, 2008), angle of attack (Yarusevych et al., 2009) and freestream turbulence level (Balzer & Fasel, 2016; Hosseinverdi & Fasel, 2019) on the nature of LSBs. However, the study of LSBs under unsteady conditions is rather limited. This is especially relevant for UAVs, that may operate in gusty environments. This problem is aggravated by the recent shift toward composite manufacturing. When subjected to unsteady aerodynamic loads, composite wings will deform considerably more than traditional lower aspect ratio structures manufactured with conventional materials. For a sinusoidal pitching airfoil, Rudmin et al. (2013) and Nati et al. (2015) observed a hysteresis cycle associated with the LSB evolution. During pitch-up, the bubble appeared further downstream compared to the static situation, while the opposite occurred during pitch-down.

From an experimental perspective, the occurrence of a LSB has been studied using various different flow measurement techniques. Boutilier & Yarusevych (2012) extracted the characteristic locations of a LSB from static pressure distributions. The presence of the bubble is indicated by the pressure plateau that forms after flow separation, followed by a region of fast pressure recovery accompanying flow reattachment (O'Meara & Mueller, 1986). Velocity measurements in the region of the bubble can be also used for characterization, as for example using Hot-Wire Anemometry (Watmuff, 1999), Laser Doppler Velocimetry (Lang et al., 2004) or Particle Image Velocimetry (PIV, see the work of Michelis et al. (2017) or Kurelek et al. (2018) for example). Surface techniques, such as Hot-Film Anemometry (Lee & Basu, 1998) or Temperature-Sensitive Paint (TSP) (Miozzi et al., 2019) have also been explored for the studying the LSB, with the advantage of giving direct information at the aerodynamic surface of interest. In this regard, Infrared Thermography (IT) has gained recent attention. As an optical technique, IT offers a higher spatial resolution than hot-films, and is considerably more simple to operate than TSP. Modern infrared cameras, with improved thermal sensitivity and temporal resolution, allow tackling studies of low-speed boundary layer (BL) transition. Wynnychuk & Yarusevych (2020) were able to extract the three characteristic locations of a steady LSB using IT, showing good agreement with PIV results. The wall-temperature measurements can be linked to the heat transfer coefficient governing the convection process with the flow and therefore be used to extract the behaviour of the BL in the region of the bubble.

For unsteady incompressible flows, surface temperature typically does not only depend on the instantaneous convective heat transfer but also on the thermal responsiveness of the surface material itself (Wolf et al., 2020). To overcome this limitation, Raffel & Merz (2014) recently proposed Differential Infrared Thermography (DIT). The principle of the technique is to subtract two subsequently recorded infrared images and then identify the instantaneous transition region from the differential image. It could be observed that, for small time separation between images, the change in transition location due to the aerodynamic unsteadiness causes a visible temperature change, whereas

no temperature changes occur for regions of the flow that remain mainly unchanged. The technique was first introduced for a pitching airfoil and compared to other experimental techniques by Wolf et al. (2019), and later extended to study the unsteady transition phenomenon for a helicopter rotor in forward flight (A. Gardner et al., 2021). For the pitching airfoil case, the experiment was replicated using thermal simulations (A. D. Gardner et al., 2017) to investigate the effect of surface material properties or image time separation on the DIT results, among other parameters. This approach showed that there is still a lag due to the thermal responsiveness of the surface, which causes an increasing error in the detected transition location for larger time separations between the subtracted images.

This study investigates the applicability of DIT to study an unsteady LSB. The wind tunnel facility and experimental techniques employed are first discussed in Sec. 2. Section 3 covers the characterization of steady LSBs for a range of angles of attack, before discussing the unsteady measurements in Sec. 4. Finally, a conclusion to the present study is given in Sec. 5.

2. Experimental procedures

2.1. Wind tunnel setup

Experiments are conducted in the Arizona Low Speed Wind Tunnel (ALSWT), situated in the Department of Aerospace and Mechanical Engineering at The University of Arizona. The closed loop facility has a test section of 0.91 m x 1.22 m x 3.66 m (height x width x length). Uniformity of the mean flow over the test section is at or better than 0.5 % and turbulence intensity is less than $Tu = 0.035\%$ in the range of 1 Hz to 10 kHz for the conditions considered here (Borgmann et al., 2020). Temperature inside the tunnel is regulated by a heat exchanger with a chilled water supply. Throughout the experiments, temperature is held within the range of 0.55 °C of 22.2 °C. A Pitot tube is mounted 0.4 m downstream of the test section entry at the tunnel side wall reaching into the free stream to acquire total and static pressures to determine the flow speed and as a reference for static pressure measurements.

A modified NACA 64_3-618 airfoil of the Aeromot 200S Super Ximango motor glider (the modified airfoil has a higher maximum lift coefficient than the original NACA 64_3-618) is used in the current investigation (Grille Guerra et al., 2021). The instrumented wind tunnel model made of carbon fiber is constructed in-house at The University of Arizona. The chord length is 1 ft (304.8 mm) and the span is 4 ft. The experiments are conducted at a chord-based Reynolds number of $Re = 200k$, which corresponds to a freestream speed inside the test section of 10.8 $\mathrm{m/s}$. As discussed by Grille Guerra et al. (2022), a LSB forms on the suction side of the wing at these conditions, covering approximately 25% of the chord.

A VELMEX BiSlide stepping motor is connected to the wing spar at 40% of the chord using a simple wheel-crank mechanism to change the angle of attack (α). This creates a constant pitching motion. The pitching rate can be easily adjusted by setting the rpm of the stepping motor. The

motor is controlled using a VELMEX VXM-1 controller, which can simultaneously output a trigger signal at desired locations of the motion. This signal is used for phase-averaging of the static pressure measurements and triggering of the infrared camera. In this investigation, the wing is pitched between -3 and 7 degrees α (5 degrees amplitude), both up and down. At $\alpha = 2$ degrees (middle of the motion), the aerodynamic pitching moment is zero at the location of the pitching axis (40% chord). This creates a symmetric motion around that point and minimizes the aerodynamic loading on the pitching mechanism.

In the experiments, the imposed motion amplitude is slightly above 5 degrees to ensure that the motor reaches a constant speed in the desired range. The time that it takes to travel the full pitching ramp (from -3 to 7 degrees α or vice versa) is used to define a motion period (as double that time) and from there a reduced frequency k, with $k = \dfrac{\pi f c}{U_\infty}$, that characterizes the motion. Here, f is the motion frequency (inverse of the period), c is the airfoil chord and U_∞ is the freestream speed inside the test section. Various reduced frequencies have been tested to increase the complexity of the motion from a quasi-steady situation to a fully unsteady case.

The experimental setup with all its relevant components is illustrated in Fig. 1. Detailed descriptions of the surface pressure and infrared measurement systems are given in the following.

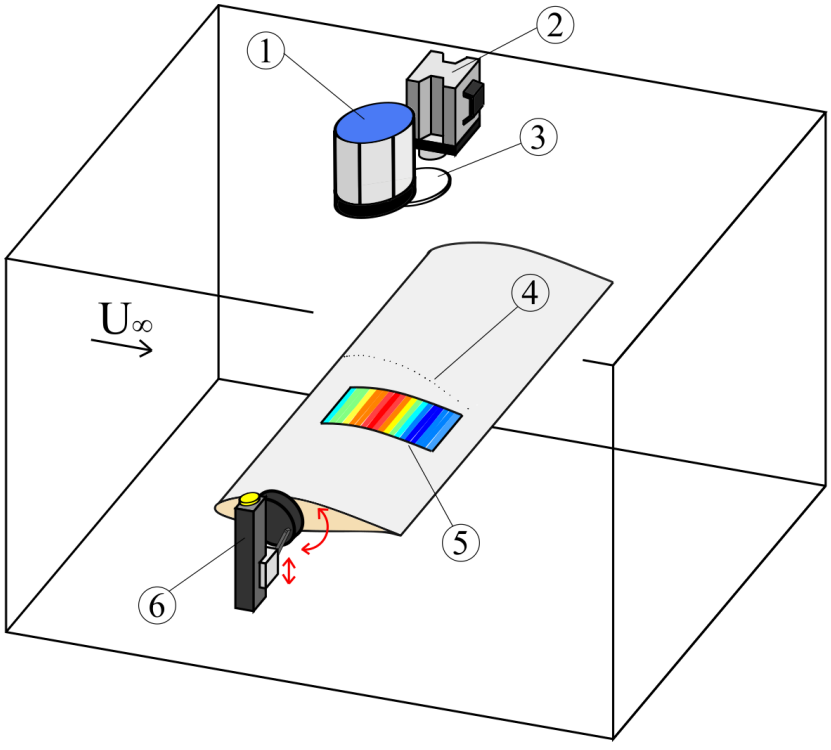

Figure 1. Sketch of the experimental setup. 1- Halogen lamp; 2- Infrared camera; 3- Ceiling aperture for infrared access; 4- Mid-span pressure taps; 5- Region of interest for IT; 6- Pitching mechanism.

2.2. Surface pressure measurements

The airfoil model contains 60 pressure taps for static pressure measurements. 36 of those are located along the chord at mid-span, as shown in Fig. 2, whereas the remaining 24 are located at 1/4 and 3/4 span, to assess the three-dimensionality of the flow. For the range of angles of attack investigated, a two-dimensional behaviour was consistently observed, and therefore only the results at mid-span will be discussed here. Scanivalve ZOC33 pressure scanners in combination with an ERAD Remote A/D module, with a range of 10 $\mathrm{inH_2O}$ (2490 Pa) are used to record static pressure. The system is sampled at 504 Hz, during 10 s for static situations and 200 s for pitching investigations.

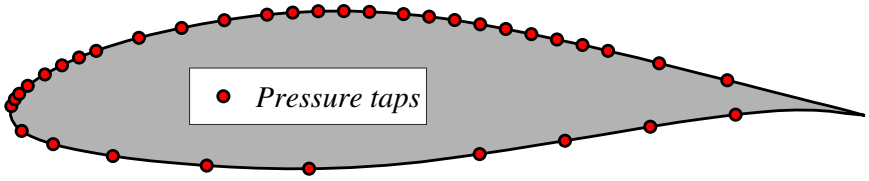

Figure 2. Distribution of pressure taps along the chord at mid-span.

Phase-averaging of the data for the pitching airfoil is accomplished by simultaneously acquiring a trigger signal from the stepping motor controller sent at $\Delta\alpha = 1^\circ$ increments. The accuracy of the system is given as ±0.1% of the measurement range. The uncertainty of the pressure measurements is estimated (with a 95% confidence interval, and following the description of Moffat (1988)) to be less than 4% of the freestream dynamic pressure (q_∞) for static configurations, while this value increases up to 7% for pitching situations. Uncertainty representation is omitted in the static pressure distribution results for improved visualization.

2.3. Infrared thermography measurements

The surface temperature on the suction side of the wing is measured using a state-of-the-art infrared camera sensitive in the MWIR band. Different cameras were used for the steady case and for the pitching investigation. An overview of the infrared camera specifications is shown in Table 1. The camera specifications are similar, but the camera used for the unsteady investigation has a higher frame rate, whereas the camera used for the steady measurements has a larger spatial resolution. The infrared cameras were not specifically temperature calibrated for this experiment. The factory calibration was used to get a rough estimate of the global temperature of the heated surface, but in the image processing stage only the infrared intensity measured directly by the sensor was considered. For the small temperature changes considered here, the calibration is quasi-linear and therefore the intensity distribution resembles well that of the temperature.

Table 1. Infrared camera specifications

	Static	Pitching
Camera model	FLIR X8501sc	FLIR X6903sc
Spectral range	3 - 5 μm	3 - 5 μm
Thermal sensitivity (NETD)	<30 mK	<20 mK
Sampling rate	50 Hz	180 Hz
Number of images	500	variable
Integration time	0.5 ms	2.8 ms
Lens focal length	50 mm	25 mm
Sensor resolution	1280 $\times$ 1024 px	640 $\times$ 512 px
$f_{\#}$	2.5	4

The IT configuration is shown in Fig. 3. In the region of interest, a thin film with low thermal conductivity was added to the airfoil skin, to increase surface emissivity and reduce conduction effects at the surface and into the wing inner structure. The wing was heated externally using a 1 kW halogen lamp placed above the WT test section, to enhance the heat transfer by convection between the surface and the flow. For infrared optical access, a small orifice was made in the acrylic ceiling.

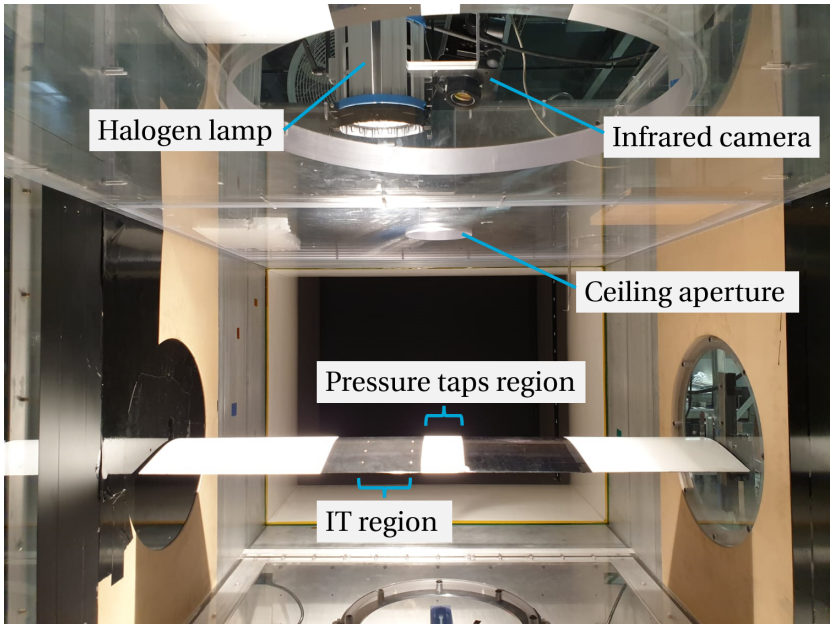

Figure 3. Test section of the ALSWT during a static IT measurement.

For the static measurements, the surface was first heated to around 10 K above ambient in quiescent conditions, and the WT was then started with the halogen lamp still turned on. When a steady-state temperature distribution was achieved (approximately 1 minute after the WT speed

settled), 500 images were sampled at 50 Hz for time-averaging. Assuming that the airfoil skin behaves as a perfect thermal insulator (von Hoesslin et al., 2017), and given the small temperature changes considered, the irradiation coming from the external heat source is simply balanced by the convective heat transfer between the surface and the flow. For convection-dominated flows, changes in heat transfer are inversely proportional to those in surface temperature. The measured temperature distributions (or heat transfer) cannot be directly linked to the momentum BL inside the bubble as the Reynolds analogy is not valid for separated flows. As suggested by Wynnychuk & Yarusevych (2020), the approach considered here is to follow the observations from Spalart & Strelets (2000), who conducted a DNS for the case of a LSB, showing the comparison between skin friction and heat transfer coefficient distributions.

In the pitching investigation, pitch up and pitch down were studied separately. For a pitch up case, the wing was first moved to an angle of attack below the minimum of the motion of interest ($\alpha = 2^\circ \pm 5^\circ$) until a steady-state was reached. The pitch up motion was then started and the infrared camera was triggered by the stepping motor controller when α reached the beginning of the constant pitch ramp ($\alpha = -3^\circ$). From there, the camera sampled at 180 Hz until $\alpha = 7^\circ$ was reached. This way, the LSB is expected to move only in one direction during the acquisition (upstream for a pitch up case), simplifying the analysis of the thermal response of the surface. An analogous procedure was used to study the pitch down configuration.

The raw infrared images are dewarped by applying an image transformation constructed with the known location of copper tape fiducial markers. These appear as dark squares in the infrared images due to the low emissivity of the material. The application of a projective transformation to the raw image example shown in Fig. 4(*a*) gives the dewarped image in Fig. 4(*b*). This image is now aligned with the flow in a coordinate system defined by the chord and spanwise directions ($x - z$). The dewarped marker locations are also used to define a rectangular region of interest (shown in cyan). This region, centred between the two rows of markers, has a width of 25% of the airfoil chord. The markers were placed such that the LSB is expected to always be inside this region. In the following, every infrared intensity distribution will be restricted to this region of interest.

3. Static characterization of the LSB

This section presents a characterization of the LSB over a range of static angles of attack, in one-degree increments, between $-3^\circ \leq \alpha \leq 7^\circ$.The presence of the LSB forming on the suction side of the wing may be identified from c_p distributions, as shown in Fig. 5 for $\alpha = -3^\circ$, 2° and 7°. Flow separation causes the formation of a pressure plateau, followed by a region of quick pressure recovery after the transition process that leads to the reattachment of a turbulent BL. To improve the spatial resolution of the pressure taps, the characteristic locations of the bubble are estimated to occur at the intersection of four linear fits constructed using the experimental data (Boutilier & Yarusevych, 2012). The results shown in Fig. 5 indicate an upstream shift of the bubble with

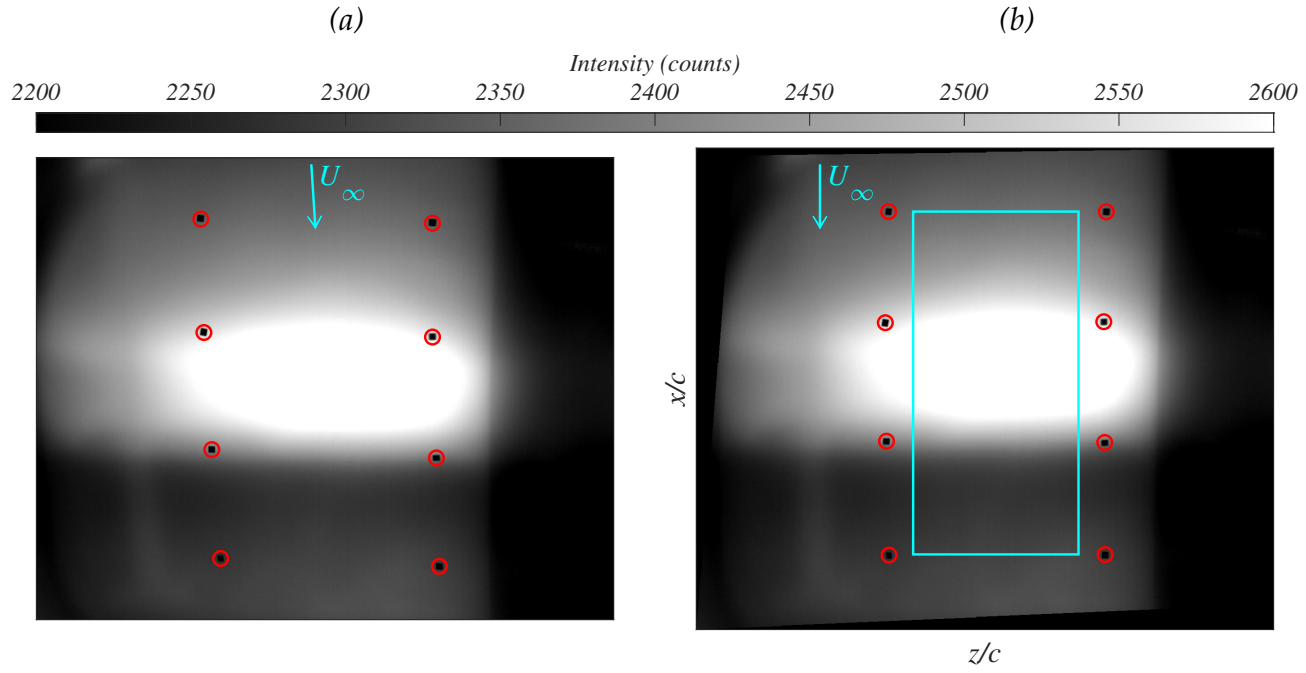

Figure 4. Infrared images containing the detected markers for image dewarping. (*a*) Raw image. (*b*) Transformed image, showing the rectangular region of interest.

increasing α, caused by a stronger adverse pressure gradient, but also illustrate the limitation of the technique for negative α due to the poor distribution of pressure taps closer to the trailing edge. This compromises the identification of transition and reattachment when these locations move too far downstream.

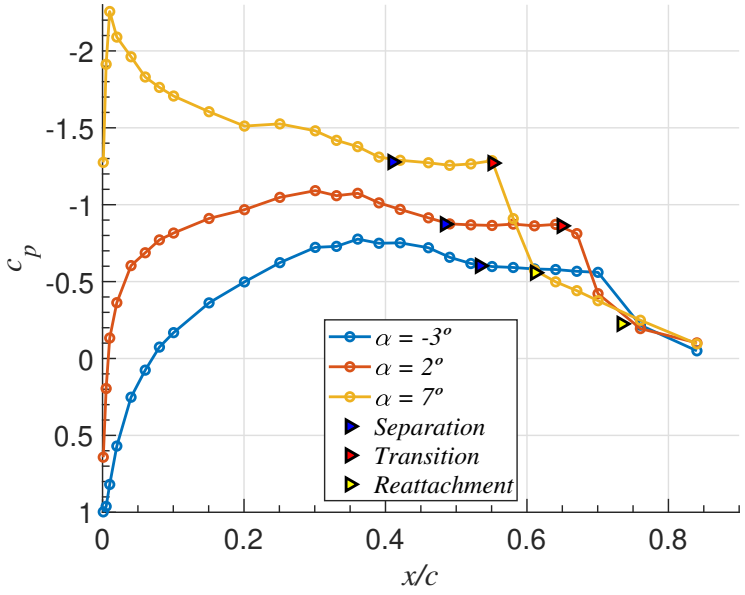

Figure 5. LSB characteristic locations estimated from c_p distributions, for the static wing at $\alpha = -3$, 2 and 7 degrees.

An alternative technique considered in this study to characterize the LSB is IT. The time-averaged infrared radiation intensity measured at the suction side of the wing, for $\alpha = 2°$, is shown in the top part of Fig. 6(*a*). A 3D distribution is observed along the span, caused by the inhomogeneous irradiation from the halogen lamp, but does not interfere with the identification of the bubble. The LSB characteristic locations are obtained at each pixel row along the span (black and white lines). The obtained distribution agrees well with the qualitative discussion extracted from Spalart & Strelets (2000). Surface temperature (or infrared radiation intensity) is observed to increase in the laminar region, achieving a maximum in the upstream part of the bubble. The temperature then starts to decrease due to the effect of transition, which continues until it reaches a minimum when the turbulent BL reattaches. Subsequently, the temperature starts to slowly increase again as the attached BL develops.

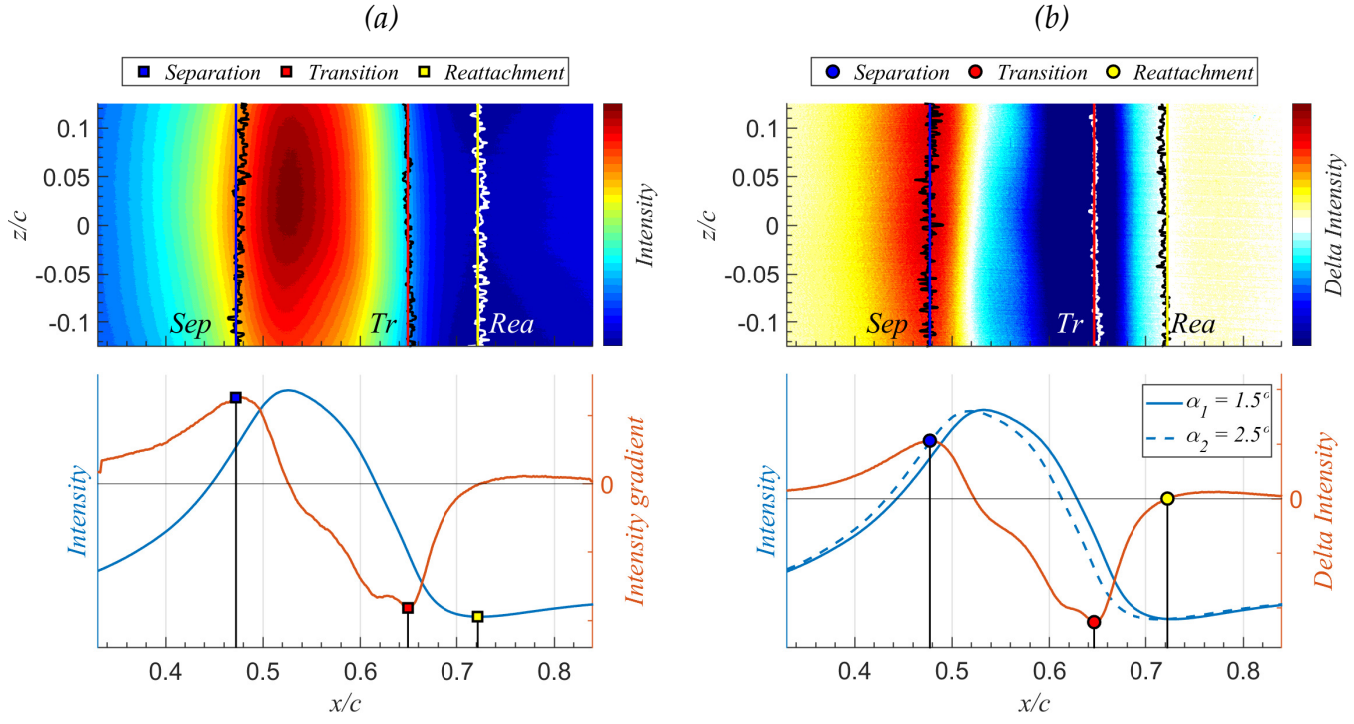

Figure 6. (*a*) Contours of time-averaged infrared intensity (top) and spanwise-averaged infrared intensity and intensity gradient distributions along the chord (bottom) for the static wing at $\alpha = 2°$. (*b*) Contours of the difference in infrared intensity between $\alpha_1 = 1.5°$ and $\alpha_2 = 2.5°$ (top) and spanwise-averaged infrared intensity and DIT distributions along the chord (bottom).

The observed 2D nature of the LSB justifies the spanwise-averaging of the intensity distribution, as a means to reduce pixel noise. The obtained intensity distribution along the chord of the airfoil is shown on the bottom part of Fig. 6(*a*). The numerical gradient of the intensity curve is also shown here, to visualize the estimation of the LSB characteristic locations extracted from those curves.

The DIT method, developed to extend the capabilities of infrared imaging inside unsteady regimes, can also be applied to static measurements (Wolf et al., 2019). For the first time, this method is extended here to study the presence of a LSB. This consists of subtracting two temperature

distributions obtained at a slightly different α and extracting the LSB characteristic locations from the differential image. The DIT distribution obtained when subtracting the static infrared intensity at $\alpha_1 = 1.5°$ from the one at $\alpha_2 = 2.5°$ is shown in Fig. 6(*b*). The LSB characteristic locations obtained from the spanwise-averaged curve represent the bubble at the intermediate value of α, this is, at $\alpha = \frac{\alpha_1 + \alpha_2}{2} = 2°$ (Richter et al., 2016).

Following the DIT argumentation first discussed by Raffel & Merz (2014), the transition location appears as a peak in the differential image due to the change in heat transfer between laminar and turbulent BLs. A similar argument can be still be made for the case of a LSB. Here, as the bubble moves upstream with increasing α, transition appears as a negative peak in the spanwise-averaged DIT distribution. The argument for laminar separation is analogous but of opposite sign. Turbulent reattachment is estimated to occur where the static distributions intersect (or where the DIT image reaches zero).

The static IT and DIT approaches are further compared in Fig. 7, by showing spanwise-averaged distributions at $\alpha = -1$, 2 and 5 degrees. As in the example above, the DIT curves are constructed using a 1-degree difference in α between thermograms.

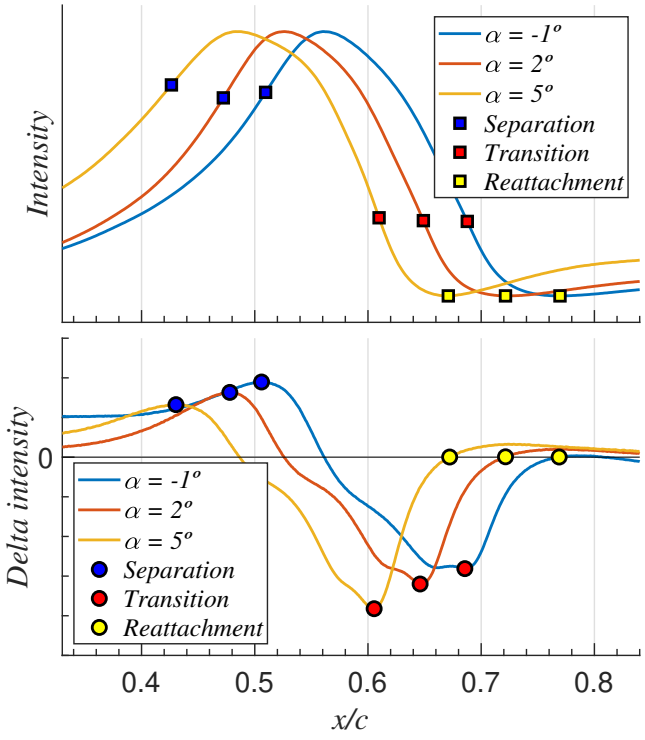

Figure 7. LSB characteristic locations estimated from spanwise-averaged IT (top) and DIT (bottom) distributions, for the static wing at $\alpha = -1$, 2 and 5 degrees.

The characteristic locations of the bubble show good agreement between the two infrared approaches. The comparison is extended to the full range of static angles of attack considered, from

$\alpha = -3°$ to $\alpha = 7°$, as shown in Fig. 8. The locations obtained from the static c_p distributions are also included in the comparison. In general, all-three techniques capture an upstream shift of the bubble with increasing incidence, showing deviations of less than 2% of the chord in the locations measured. As discussed earlier, some information is missing from the pressure taps in the negative incidence region due to the lack of taps in this area of the wing.

The results presented in this section confirm the validity of DIT to study the case of a LSB and motivate its exploration for unsteady regimes. For static measurements, the infrared approach outperforms the surface pressure measurements, thanks to the improved spatial resolution of the technique. The time-averaged infrared images provide a deeper description of the flow feature, showing the behaviour along the span. In the current investigation, the 2D nature of the flow offers the possibility of using a spanwise-averaging of the measurements to reduce pixel noise.

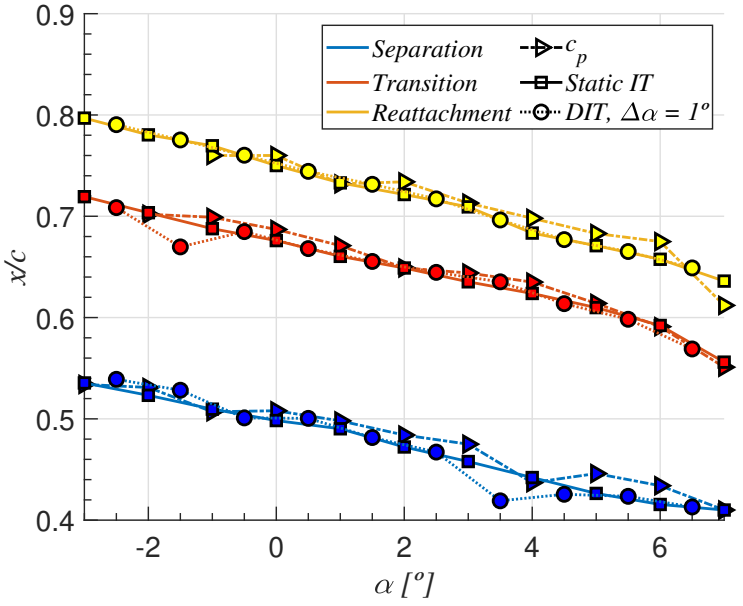

Figure 8. Comparison of the LSB characteristic locations measured using IT, DIT and c_p distributions, for the static wing between $\alpha = -3°$ and $\alpha = 7°$.

4. Unsteady LSB behaviour

This section presents the results of the pitching investigation, conceived to explore the capabilities of DIT for the detection of an unsteady LSB. The motion imposed to the wing consists of pitch up and pitch down ramps at a constant pitch rate, between $\alpha = -3°$ and $\alpha = 7°$, as described in Sec. 2. Different degrees of unsteadiness are investigated, up to $k = 0.25$, by changing the pitch rate $\dot{\alpha}$ to assess the performance of the experimental techniques.

A first comparison between pitch up and pitch down is shown in Fig. 9, using phase-averaged static pressure coefficient distributions for the pitching wing at $\alpha = 2°$. The results indicate a hysteresis in bubble location between pitch up and pitch down, illustrated by the transition location

estimation, which is obtained following the same methodology as for the static investigation. Transition is observed to occur slightly upstream during pitch down, which is in agreement with the experimental results of Nati et al. (2015) for a sinusoidally pitching airfoil.

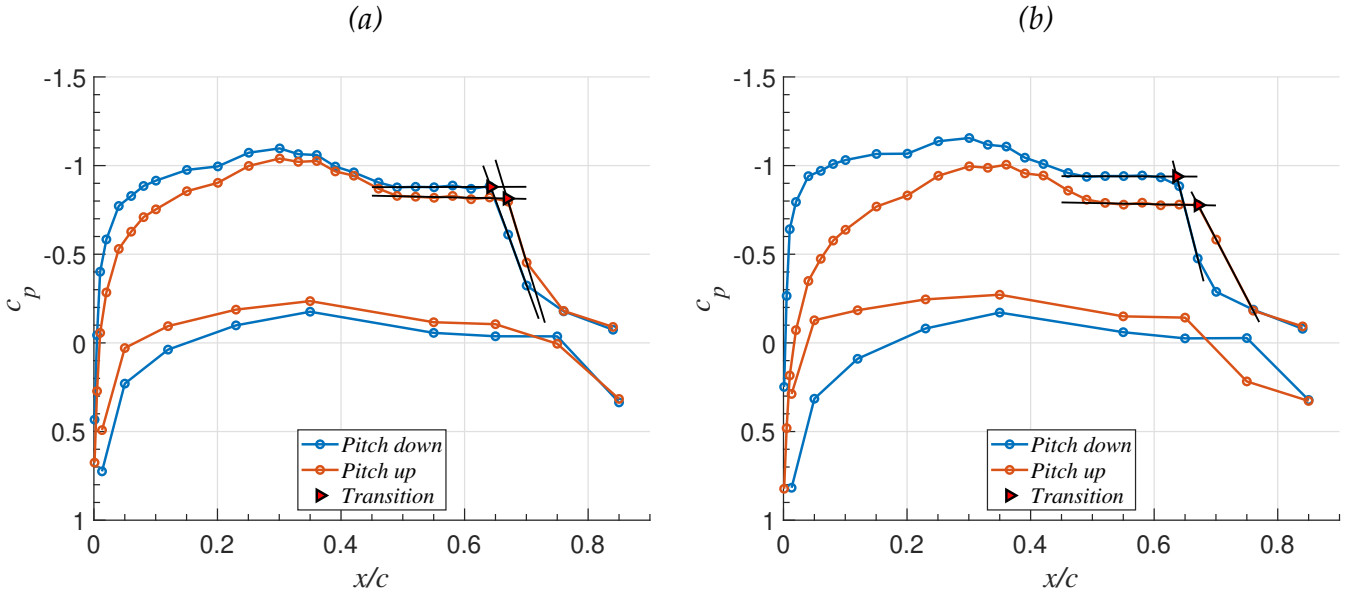

Figure 9. Phase-averaged c_p distributions for the pitching wing at $\alpha = 2°$, both for pitch up and pitch down, with: (*a*) $k = 0.05$ and (*b*) $k = 0.15$.

From an experimental perspective, the increase in reduced frequency does not affect the surface pressure measurements. Using a phase-averaged approach, the technique can be operated at motion frequencies much higher than the ones considered here. However, this may not be the case for DIT. To illustrate the performance of the technique, DIT curves are constructed, centred at $\alpha = 2°$, using a 1-degree difference between thermograms, as for the static approach discussed in Sec. 3. As the pitch rate $\dot{\alpha}$ increases, the time difference between thermograms needs to be decreased to keep this value constant. DIT curves, obtained during pitch up for four different reduced frequencies, are shown in Fig. 10(*a*), while the results obtained during pitch down are shown in Fig. 10(*b*).

The pitch up curves show a negative DIT peak associated with the unsteady transition location, visible for every frequency. This location is always downstream of the static value (in agreement with surface pressure measurements), with the difference increasing with frequency as expected. The strength of the DIT peak generally decreases with increasing frequency, as the physical time between DIT frames reduces (please note that, for $k = 0.25$, the difference between thermograms is slightly higher than one degree, due to limited availability). However, no clear positive peak is visible upstream of transition, expected to indicate the unsteady separation location. Similarly, measurement noise downstream of transition obscures the identification of the reattachment location.

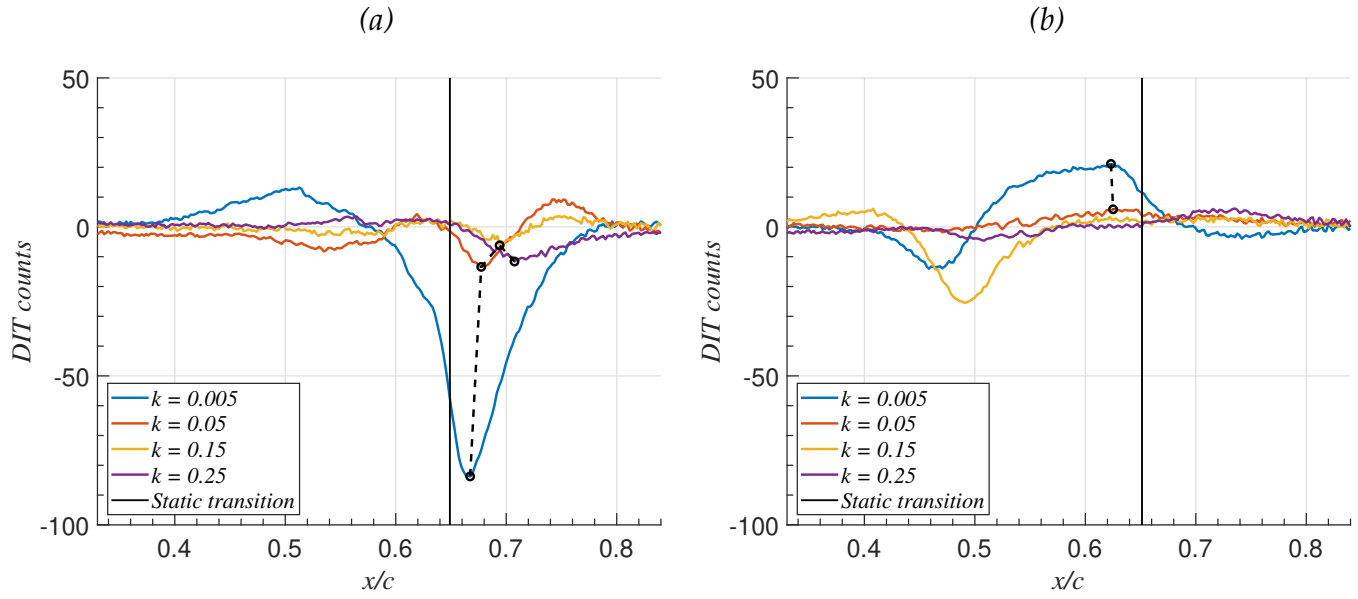

Figure 10. DIT curves for the pitching wing at $\alpha = 2°$, for various motion reduced frequencies and using a separation between thermograms of one degree, during (*a*) pitch up (*b*) pitch down.

A different behaviour is observed during pitch down. Now, unsteady transition appears as a positive DIT peak, caused by the change in direction of the bubble. This feature could only be detected for small motion frequencies, but does appear upstream of the static location. The obtained results suggest that DIT performs better during pitch up. In the transition region, the flow changes from laminar to turbulent when considering a pitch up motion, thus enhancing surface cooling through convection.

The comparison between reduced frequencies can be extended beyond $\alpha = 2°$ to obtain the continuous transition location at every angle of attack along the motion. The results obtained for every reduced frequency tested are included in Fig. 11(*a*). A quasi-steady measurement, that corresponds to a reduced frequency of $k = 0.0002$, is included to represent the static transition location. The pitch up curves show transition downstream of the static value at the same incidence, in agreement with previous studies (see for example Pascazio et al. (1996) or Lee & Basu (1998)). The results during pitch down are inconclusive, being similar for every motion frequency available.

The DIT results are compared to those from the pressure taps in terms of the hysteresis in transition location. This is typically defined as the difference between the pitch up and pitch down case. However, very limited information could be obtained from pitch down using DIT. To overcome this limitation, hysteresis is defined here individually for each case, based on the static transition location. The obtained results are shown in Fig. 11(*b*), for the wing at $\alpha = 2°$, in terms of the reduced frequency of the motion or constant pitch rate ($\dot{\alpha}$) imposed.

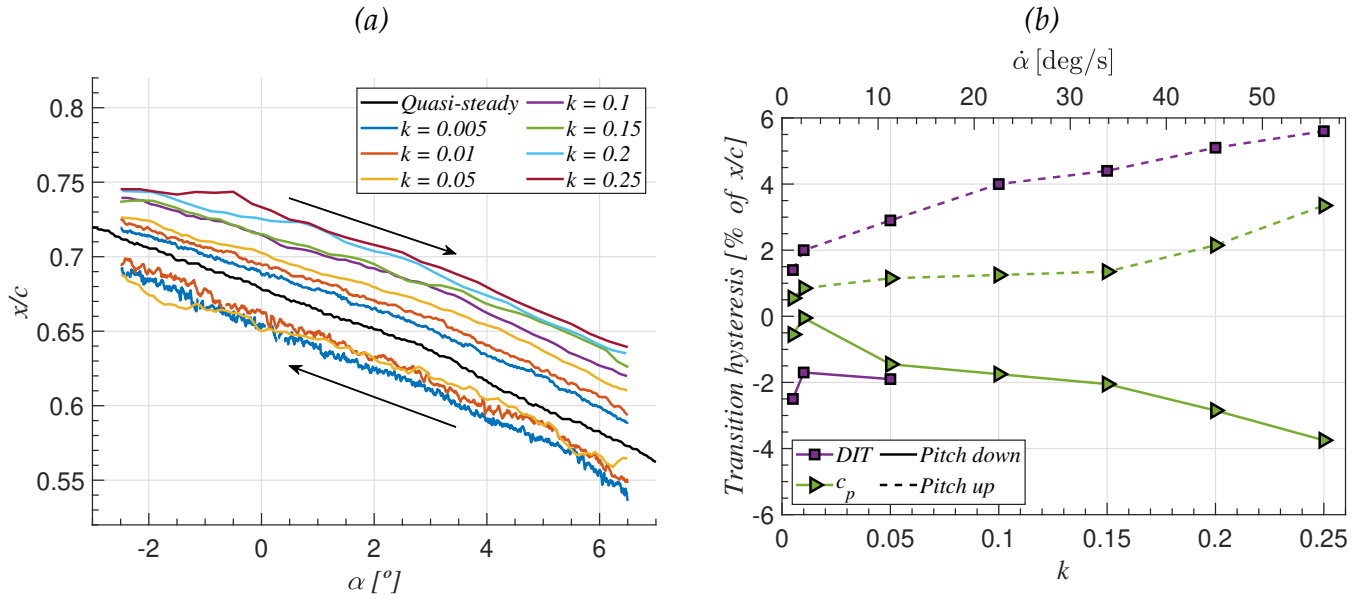

Figure 11. Unsteady transition location for the pitching wing, obtained from DIT (*a*), and hysteresis in transition location (*b*).

The surface pressure measurements suggest that hysteresis is approximately symmetric between pitch up and pitch down, with the value increasing almost linearly for the range of motion frequencies considered here. Instead, the hysteresis measured with DIT (for pitch up) increases rapidly before reaching a linear evolution that shows a higher value than the previous (approximately 3% higher). This behaviour is analogous to that measured by Wolf et al. (2019) for a sinusoidally pitching airfoil at a higher Reynolds number. As discussed by Richter et al. (2016), who compared DIT with hot-film sensors and pressure transducers, this additional hysteresis is argued to be caused by the thermal lag of the model surface.

5. Conclusion

The LSB that forms on the suction side of a modified NACA 6-series airfoil at a chord-based Reynolds number of $Re = 200k$ has been studied in a series of wind tunnel experiments using surface pressure measurements and infrared thermography. The presence and nature of the bubble was analyzed through the identification of three characteristic locations that define this flow feature: the separation of the laminar boundary layer, the transition to turbulence in the separated shear layer, and the subsequent reattachment of the turbulent boundary layer. The LSB was first characterized over a range of static angles of attack, using one-degree increments, between $-3° \leq \alpha \leq 7°$. Both techniques indicated an upstream shift of the bubble with increasing incidence. The LSB was for the first time also identified using an extension of the DIT method, establishing the validity of this technique. For the study of steady LSBs, the infrared approach is superior, given its higher spatial resolution, experimental simplicity and the possibility of inspecting the 3-dimensionality of the flow.

A pitching-type motion, of the form $\alpha = 2^\circ \pm 5^\circ$, was applied to the wind tunnel model to study the capabilities of the DIT method in detecting an unsteady LSB. For the reduced frequencies tested (up to $k = 0.25$), the technique could only detect the effects of the unsteady transition process, indicating a hysteresis between pitch up and pitch down parts of the motion. The low level of convective heat transfer associated with the presence of a LSB compromises the applicability of the technique to small amounts of aerodynamic unsteadiness. Furthermore, the hysteresis in transition location measured with DIT is higher than the one measured with the pressure taps, which is argued to be caused by the additional thermal lag of the surface. This behaviour is in agreement with previous research on the use of DIT for unsteady transition detection.

This study demonstrates the suitability of DIT to study different unsteady flow phenomena, and the range is expected to continue increasing in the future. Even if modern infrared cameras can provide high levels of temporal resolution, for the application of DIT the thermal response of the surface is of key importance, which is governed by a combination of material properties and the changes in convective heat transfer associated with the unsteady problem of interest. Both aspects need to be carefully inspected prior to the experiments, as these will limit the applicability of the DIT method.

Acknowledgements

This work was supported by the Air Force Office of Scientific Research (AFOSR) under grant number FA9550-19-1-0174 with Dr. Gregg Abate serving as the program manager. The authors wish to thank Prof. S. Craig of The University of Arizona for the use of the infrared camera.

Nomenclature

c	Airfoil chord [m]
c_l	Lift coefficient [-]
c_p	Static pressure coefficient [-]
f	Frequency [Hz]
k	Reduced frequency [-]
q_∞	Freestream dynamic pressure [Pa]
Re	Reynolds number [-]
U_∞	Freestream speed [m s^{-1}]
x	Chordwise direction [m]
z	Spanwise direction [m]
α	Angle of attack [deg]
$\dot{\alpha}$	Pitch rate [deg s^{-1}]

References

Balzer, W., & Fasel, H. F. (2016). Numerical investigation of the role of free-stream turbulence in boundary-layer separation. *Journal of Fluid Mechanics*, *801*, 289–321. doi: 10.1017/jfm.2016.424

Borgmann, D., Hosseinverdi, S., Little, J., & Fasel, H. (2020). Investigation of low-speed boundary-layer instability and transition using experiments, theory and DNS. *AIAA Aviation Forum*. doi: 10.2514/6.2020-2948

Boutilier, M. S., & Yarusevych, S. (2012). Parametric study of separation and transition characteristics over an airfoil at low Reynolds numbers. *Experiments in Fluids*, *52*(6), 1491–1506. doi: 10.1007/s00348-012-1270-z

Burgmann, S., & Schröder, W. (2008). Investigation of the vortex induced unsteadiness of a separation bubble via time-resolved and scanning PIV measurements. *Experiments in Fluids*, *45*(4), 675–691. doi: 10.1007/s00348-008-0548-7

Gardner, A., Weiss, A., Heineck, J., Overmeyer, A., Spooner, H., Jain, R., … Raffel, M. (2021). Boundary Layer Transition Measured by DIT on the PSP Rotor in Forward Flight. *Journal of the American Helicopter Society*, *022008*(July 2020), 1–10. doi: 10.4050/jahs.66.022008

Gardner, A. D., Eder, C., Wolf, C. C., & Raffel, M. (2017). Analysis of differential infrared thermography for boundary layer transition detection. *Experiments in Fluids*, *58*(9), 1–14. doi: 10.1007/s00348-017-2405-z

Gaster, M. (1967). The Structure and Behaviour of Laminar Separation Bubbles. *Aeronautical Research Council Reports and Memoranda*, *3595*, 1–31.

Grille Guerra, A., Hosseinverdi, S., Little, J., & Fasel, H. F. (2022). Unsteady Behavior of a Laminar Separation Bubble Subjected to Wing Structural Motion. *AIAA SciTech Forum*, 1–17. doi: 10.2514/6.2022-2331

Grille Guerra, A., Hosseinverdi, S., Singh, A., Little, J., & Fasel, H. (2021). Unsteady Evolution of a Laminar Separation Bubble Subjected to Structural Motion. *AIAA Aviation Forum*, 1–18. doi: 10.2514/6.2021-2949

Horton, H. (1968). *Laminar Separation Bubbles in Two and Three Dimensional Incompressible Flow* (Unpublished doctoral dissertation). University of London.

Hosseinverdi, S., & Fasel, H. F. (2019). Numerical investigation of laminar-turbulent transition in laminar separation bubbles: The effect of free-stream turbulence. *Journal of Fluid Mechanics*, *858*, 714–759. doi: 10.1017/jfm.2018.809

Kurelek, J. W., Kotsonis, M., & Yarusevych, S. (2018). Transition in a separation bubble under tonal and broadband acoustic excitation. *Journal of Fluid Mechanics*, *853*, 1–36. doi: 10.1017/jfm.2018.546

Lang, M., Rist, U., & Wagner, S. (2004). Investigations on controlled transition development in a laminar separation bubble by means of LDA and PIV. *Experiments in Fluids*, *36*(1), 43–52. doi: 10.1007/s00348-003-0625-x

Lee, T., & Basu, S. (1998). Measurement of unsteady boundary layer developed on an oscillating airfoil using multiple hot-film sensors. *Experiments in Fluids*, *25*(June 1997), 108–117.

Michelis, T., Yarusevych, S., & Kotsonis, M. (2017). Response of a laminar separation bubble to impulsive forcing. *Journal of Fluid Mechanics*, *820*, 633–666. doi: 10.1017/jfm.2017.217

Miozzi, M., Capone, A., Costantini, M., Fratto, L., Klein, C., & Di Felice, F. (2019). Skin friction and coherent structures within a laminar separation bubble. *Experiments in Fluids*, *60*(1), 1–25. doi: 10.1007/s00348-018-2651-8

Moffat, R. J. (1988). Describing the uncertainties in experimental results. *Experimental Thermal and Fluid Science*, *1*(1), 3–17. doi: 10.1016/0894-1777(88)90043-X

Nati, A., de Kat, R., Scarano, F., & van Oudheusden, B. W. (2015). Dynamic pitching effect on a laminar separation bubble. *Experiments in Fluids*, *56*(9), 1–17. doi: 10.1007/s00348-015-2031-6

O'Meara, M. M., & Mueller, T. J. (1986). Experimental Determination of the Laminar Separation Bubble Characteristics of an Airfoil At Low Reynolds Numbers. *AIAA Paper*, *25*(8). doi: 10.2514/6.1986-1065

Pascazio, M., Autric, J. M., Favier, D., & Maresca, C. (1996). Unsteady boundary-layer measurement on oscillating airfoils: Transition and separation phenomena in pitching motion. *34th Aerospace Sciences Meeting and Exhibit*. doi: 10.2514/6.1996-35

Raffel, M., & Merz, C. B. (2014). Differential infrared thermography for unsteady boundary-layer transition measurements. *AIAA Journal*, *52*(9), 2090–2093. doi: 10.2514/1.J053235

Richter, K., Wolf, C. C., Gardner, A. D., & Merz, C. B. (2016). Detection of unsteady boundary layer transition using three experimental methods. *54th AIAA Aerospace Sciences Meeting*, *0*(January), 1–22. doi: 10.2514/6.2016-1072

Rudmin, D., Benaissa, A., & Poirel, D. (2013). Detection of laminar flow separation and transition on a NACA-0012 airfoil using surface hot-films. *Journal of Fluids Engineering, Transactions of the ASME*, *135*(10), 1–6. doi: 10.1115/1.4024807

Spalart, P. R., & Strelets, M. K. (2000). Mechanisms of transition and heat transfer in a separation bubble. *Journal of Fluid Mechanics*, *403*, 329–349. doi: 10.1017/S0022112099007077

von Hoesslin, S., Stadlbauer, M., Gruendmayer, J., & Kähler, C. J. (2017). Temperature decline thermography for laminar–turbulent transition detection in aerodynamics. *Experiments in Fluids*, *58*(9), 1–10. doi: 10.1007/s00348-017-2411-1

Watmuff, J. H. (1999). Evolution of a wave packet into vortex loops in a laminar separation bubble. *Journal of Fluid Mechanics*, *397*, 119–169.

Wolf, C. C., Gardner, A. D., & Raffel, M. (2020). Infrared thermography for boundary layer transition measurements. *Measurement Science and Technology*.

Wolf, C. C., Mertens, C., Gardner, A. D., Dollinger, C., & Fischer, A. (2019). Optimization of differential infrared thermography for unsteady boundary layer transition measurement. *Experiments in Fluids*, *60*(1), 1–13. doi: 10.1007/s00348-018-2667-0

Wynnychuk, D. W., & Yarusevych, S. (2020). Characterization of laminar separation bubbles using infrared thermography. *AIAA Journal*, *58*(7), 2831–2843. doi: 10.2514/1.J059160

Yarusevych, S., Sullivan, P. E., & Kawall, J. G. (2009). On vortex shedding from an airfoil in low-Reynolds-number flows. *Journal of Fluid Mechanics*, *632*, 245–271. doi: 10.1017/S0022112009007058